

# Recollision as a probe of magnetic field effects in non-sequential double ionization

A. Emmanouilidou<sup>1</sup> and T. Meltzer<sup>1</sup>

<sup>1</sup>*Department of Physics and Astronomy, University College London,  
Gower Street, London WC1E 6BT, United Kingdom*

(Dated: March 20, 2018)

Fully accounting for non-dipole effects in the electron dynamics, double ionization is studied for He driven by a near-infrared laser field and for Xe driven by a mid-infrared laser field. Using a three-dimensional semiclassical model, the average sum of the electron momenta along the propagation direction of the laser field is computed. This sum is found to be an order of magnitude larger than twice the average electron momentum along the propagation direction of the laser field in single ionization. Moreover, the average sum of the electron momenta in double ionization is found to be maximum at intensities smaller than the intensities satisfying previously predicted criteria for the onset of magnetic field effects. It is shown that strong recollisions are the reason for this unexpectedly large value of the sum of the momenta along the direction of the magnetic component of the Lorentz force.

## INTRODUCTION

Non-sequential double ionization in two-electron atoms is a fundamental process that explores electron-electron correlation in strong fields. As such, it has attracted a lot of interest in the field of light-matter interactions in recent years [1, 2]. The majority of theoretical studies on NSDI are delivered in the framework of the dipole approximation, particularly the studies involving the commonly used near-infrared laser fields and intensities [3]. In the dipole approximation the vector potential  $\mathbf{A}$  of the laser field does not depend on space. Therefore, magnetic field effects are neglected, since the magnetic field component of the laser field  $\mathbf{B} = \nabla \times \mathbf{A}(t)$  is zero. However, in the general case where  $\mathbf{A}$  depends both on space and time, an electron experiences a Lorentz force whose magnetic field component  $\mathbf{F}_B$  increases with increasing electron velocity, since  $\mathbf{F}_B = q\mathbf{v} \times \mathbf{B}$ . It is important to account for magnetic field effects, since in strong field ionization high velocity electrons are often produced. Criteria for the onset of magnetic field effects both in the relativistic and the non-relativistic limit have already been formulated [4, 5]. In the non-relativistic limit, where this work focuses, magnetic field effects are expected to arise when the amplitude of the electron motion due to the magnetic field component of the Lorentz force becomes 1 a.u., i.e.  $\beta_0 = U_p/(2\omega c) \approx 1$  a.u. [4, 5], with  $U_p$  the ponderomotive energy.

Studies addressing magnetic field effects include using a 3D semiclassical rescattering model that accounts for  $\mathbf{F}_B$  to successfully describe the observed ionization of  $\text{Ne}^{n+}$  ( $n \leq 8$ ) in ultra-strong fields [6]. Moreover, non-dipole effects were addressed in theoretical studies of high-order harmonic generation, for instance, by neglecting the Coulomb potential [7] or by using a first order expansion of the vector potential [8]. In recent studies of single ionization (SI), the electron momentum distribution along the propagation direction of the laser field was computed using different quantum mechanical ap-

proaches [9–12]. For example, for H interacting with a 3400 nm laser field at intensities  $0.5\text{--}1 \times 10^{14} \text{ Wcm}^{-2}$  the average momentum along the propagation direction of the laser field was found to increase from 0.003 a.u. to 0.006 a.u. [10]. Thus, for single ionization, the average of this momentum component increases with increasing  $\beta_0$  [10, 13]. If magnetic field effects are not accounted for, then this momentum component averages to zero. The motivation for these theoretical studies was a recent experimental observation of the average momentum in the propagation direction of the laser field [13].

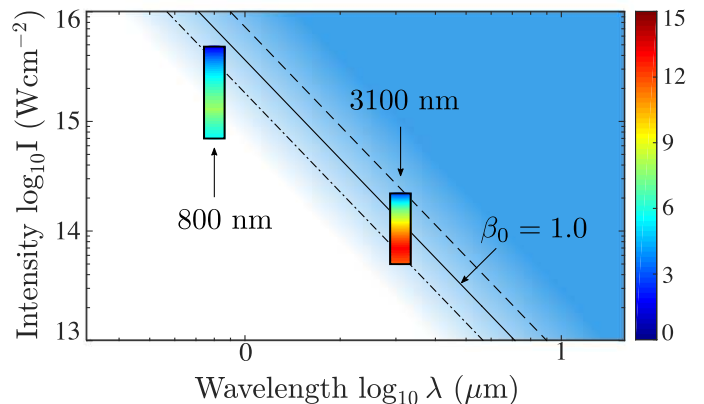


**Figure 1 | Range of validity of the dipole approximation and momentum in double ionization.** The white area indicates the range of intensities and wavelengths where the dipole approximation is valid.  $\beta_0 = 0.5$  a.u. (dot-dash line),  $\beta_0 = 1$  a.u. (solid line) and  $\beta_0 = 2$  a.u. (dash line). The arrows mark the 800 nm and the 3100 nm wavelengths driving He and Xe, respectively. At these wavelengths, for a range of intensities, the color bars indicate the ratio of the average sum of the electron momenta along the direction of  $\mathbf{F}_B$  for double ionization with twice the respective electron momentum for single ionization  $\langle p_y^1 + p_y^2 \rangle_{\text{DI}} / (2 \langle p_y \rangle_{\text{SI}})$ .

This work reveals another aspect of non-sequential double ionization (NSDI) which has not been previously addressed. The strong electron-electron correlation in

NSDI is identified as a probe of magnetic field effects both for near-infrared and mid-infrared intense laser fields. Specifically, the intensities considered are around  $10^{15}$   $\text{Wcm}^{-2}$  for He at 800 nm and around  $10^{14}$   $\text{Wcm}^{-2}$  for Xe at 3100 nm where the rescattering mechanism underlies double ionization [14]. For these intensities, it is found that the average sum of the two electron momenta along the propagation direction of the laser field is unexpectedly large. It is roughly an order of magnitude larger than twice the average of the respective electron momentum for single ionization. This average sum of the momenta for double ionization (DI) is shown to be maximum at intensities smaller than the intensities satisfying the criterion for the onset of magnetic field effects  $\beta_0 \approx 1$  a.u. [4, 5]. This is illustrated in Fig. 1 for He driven by a near-infrared (800 nm) laser field and for Xe driven by a mid-infrared (3100 nm) laser field. The motivation for choosing near-infrared laser fields is that they are very common in strong field studies. Mid-infrared laser-fields are chosen because magnetic field effects set in for small intensities, see Fig. 1, attracting a lot of interest in recent years [15, 16].

## METHOD

For the current studies, a 3D semiclassical model is employed that fully accounts for non-dipole effects during the time propagation. For simplicity this model is referred to as 3D-SMND. It is an extension of a 3D semiclassical model that was previously formulated in the framework of the dipole approximation. This latter model is referred to as 3D-SMD. Thus, in the 3D-SMND model non-dipole effects are fully accounted for in the two-electron dynamics. Some of the successes of the 3D-SMD model are identifying the mechanism responsible for the fingerlike structure [17], which was predicted theoretically [18] and was observed experimentally for He driven by 800 nm laser fields [19, 20]; investigating direct versus delayed pathways of NSDI for He driven by a 400 nm laser field while achieving excellent agreement with fully ab-initio quantum mechanical calculations [21]; identifying the underlying mechanisms for the carrier-envelope phase effects observed experimentally in NSDI of Ar driven by an 800 nm laser field at a range of intensities [22, 23]. The 3D-SMD model is extended to the 3D-SMND model employed in the current work to fully account for the magnetic field during time propagation. The Hamiltonian describing the interaction of the fixed nucleus two-electron atom with the laser field is given by

$$H = \frac{(\mathbf{p}_1 + \mathbf{A}(y_1, t))^2}{2} + \frac{(\mathbf{p}_2 + \mathbf{A}(y_2, t))^2}{2} - c_1 \frac{Z}{|\mathbf{r}_1|} - c_2 \frac{Z}{|\mathbf{r}_2|} + c_3 \frac{1}{|\mathbf{r}_1 - \mathbf{r}_2|}, \quad (1)$$

where the vector potential  $\mathbf{A}$  is given by

$$\mathbf{A}(y, t) = -\frac{E_0}{\omega} e^{-\left(\frac{ct-y}{c\tau}\right)^2} \sin(\omega t - ky) \hat{x}, \quad (2)$$

$\omega$ ,  $k$ ,  $E_0$  are the frequency, wavenumber and strength of the electric component of the laser field, respectively, and  $c$  is the velocity of light.  $\tau = \text{FWHM}/\sqrt{\ln 4}$  with FWHM the full width half maximum of the laser field. All Coulomb forces are accounted for by setting  $c_1 = c_2 = c_3 = 1$ . In this work linearly polarized laser fields are considered. To switch-off a Coulomb interaction we set the appropriate constant equal to zero, for example, to switch-off the interaction of electron 1 with the nucleus we set  $c_1 = 0$ . For  $\mathbf{A}$  given by Eq. (2),  $\mathbf{E}$  and  $\mathbf{B}$  are along the x- and z-axis, respectively, while the propagation direction of the laser field and the direction of  $\mathbf{F}_B$  are along the y-axis. Unless otherwise stated, all Coulomb forces as well as the electric and the magnetic field are fully accounted for during time propagation. Moreover, the Coulomb singularity is addressed using regularized coordinates [24] which were also employed in the 3D-SMD model [17, 21, 22].

The initial state in the 3D-SMND model is taken to be the same as in the 3D-SMD model [17, 21, 22]. It entails one electron tunneling through the field-lowered Coulomb potential with a non-relativistic quantum tunneling rate given by the Ammosov-Delone-Krainov (ADK) formula [25, 26]. The momentum along the direction of the electric field is zero while the transverse one is given by a Gaussian distribution [25, 26]. A non-relativistic ADK rate results in this Gaussian distribution being centered around zero. In ref. [27] non-dipole effects were accounted for in the ADK rate. It was shown that the most probable transverse velocity ranges from  $0.33 I_p/c$  to almost zero with increasing  $E_0/(2I_p)^{3/2}$ , with  $I_p$  the ionization energy of the tunneling electron. In this work, the smallest intensities considered are  $5 \times 10^{13}$   $\text{Wcm}^{-2}$  for Xe and  $7 \times 10^{14}$   $\text{Wcm}^{-2}$  for He. At these intensities, if non-dipole effects are accounted for in the ADK rate, the transverse velocity of the tunneling electron is centered around  $0.17 I_p^{\text{Xe}}/c$  for Xe which is  $5.5 \times 10^{-4}$  a.u. ( $I_p^{\text{Xe}} = 0.446$  a.u.) and  $0.12 I_p^{\text{He}}/c$  for He which is  $7.9 \times 10^{-4}$  a.u. ( $I_p^{\text{He}} = 0.904$  a.u.). These values are significantly smaller than the values of the average momenta along the propagation direction of the laser field, which are presented in what follows. Thus, using the non-relativistic ADK rate is a good approximation for the quantities addressed in this work. The remaining electron is initially described by a microcanonical distribution [28]. In what follows, the tunneling and bound electron are denoted as electrons 1 and 2, respectively.

## RESULTS

### $p_y$ for single ionization of Xe and H

The accuracy of the 3D-SMND model is established by computing the momentum distribution along the propagation direction of the laser field,  $p_y$ , for single ionization (SI) and by comparing it with available experimental and theoretical results. In ref. [16], the peak of the  $p_y$  distribution was observed to shift in the direction opposite to the magnetic field component of the Lorentz force,  $F_B$ , for intensities on the order of  $10^{13}$   $\text{Wcm}^{-2}$ . This shift was attributed to the combined effect of the magnetic field and the Coulomb attraction of the nucleus [16]. To compare with these experimental results, the shift of the peak of the  $p_y$  distribution is computed for Xe interacting with a 3400 nm and a 44 fs FWHM laser field as the intensity increases from  $3\text{-}6 \times 10^{13}$   $\text{Wcm}^{-2}$ . The shift of the peak of the  $p_y$  distribution is found to vary from  $-0.0055$  a.u. to  $-0.012$  a.u.. These results are in agreement with the simulations and experimental results presented in ref. [16]. Moreover, to compare with the results in ref. [10], the average of the momentum  $\langle p_y \rangle_{\text{SI}}$  is computed for H driven by a 3400 nm and a 16 fs FWHM laser field for intensities  $0.5\text{-}1 \times 10^{14}$   $\text{Wcm}^{-2}$ . Using the 3D-SMND model,  $\langle p_y \rangle_{\text{SI}}$  is found to vary from 0.0022 a.u. to 0.0046 a.u.. These values differ by 27% from the results presented in ref. [10] and are thus in reasonable agreement. The difference may be due to non-dipole effects not accounted for in the ADK rate in the 3D-SMND model. In addition, the quantum calculation used in ref. [10] employs a 2D soft-core potential while a full 3D potential is employed by the 3D-SMND model. The single ionization results obtained in this work were computed with at least  $4 \times 10^5$  events and therefore the statistical error introduced is very small.

### $\langle p_y \rangle$ for single ionization of He and Xe

The 3D-SMND model is now employed to compute  $\langle p_y \rangle_{\text{SI}}$  for He driven by an 800 nm, 12 fs FWHM laser field and for Xe driven by a 3100 nm, 44 fs FWHM laser field; the two laser fields have roughly the same number of cycles. First an analytic expression is obtained relating  $\langle p_y \rangle_{\text{SI}}$  with the average electron kinetic energy  $\langle E_k \rangle_{\text{SI}}$  [9, 13]. When an electron interacts with an electromagnetic field with all the Coulomb forces switched-off, i.e.  $c_1 = c_2 = c_3 = 0$  in Eq. (1), the equations of motion are  $\dot{p}_y = -(\mathbf{v} \times \mathbf{B})_y$  and  $\dot{p}_x = -(\mathbf{v} \times \mathbf{B})_x - E$ . Keeping only first order terms in  $1/c$ ,  $\dot{p}_x = -E$  resulting in  $p_y - p_{0,y} = p_x^2/(2c) - p_{0,x}^2/(2c)$ , with  $p_{0,x/y}$  the  $x/y$  components of the electron momentum at time  $t_0$ . The initial momentum of the tunneling electron along the electric field direction is set to zero, as in the 3D-SMND model, resulting in  $p_y - p_{0,y} = p_x^2/(2c) = E_k/c$ .

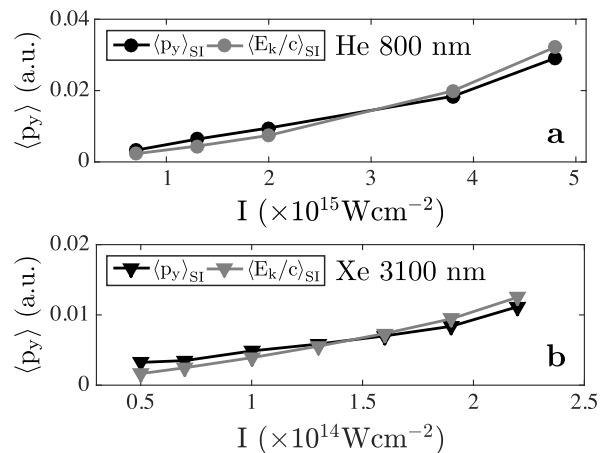


**Figure 2 | Single ionization of He and Xe.**  $\langle p_y \rangle_{\text{SI}}$  and  $\langle E_k \rangle_{\text{SI}}/c$  are plotted as a function of intensity in (a) for He driven by an 800 nm laser field and in (b) for Xe driven by a 3100 nm laser field.

Thus,  $\langle p_y \rangle = \langle p_{0,y} \rangle + \langle E_k \rangle/c$  is obtained. For this simple model  $\langle E_k \rangle$  is the drift energy of the electron. As discussed in the Method section, if non-dipole effects are accounted for in the tunneling rate then  $\langle p_{0,y} \rangle$  varies from  $0.33 I_p/c$  to almost zero with increasing intensity. In the 3D-SMND model non-dipole effects are not included in the ADK rate and therefore  $\langle p_{0,y} \rangle = 0$ . Indeed, using the 3D-SMND model with  $c_1 = c_2 = c_3 = 0$ , it is found that  $\langle p_y \rangle_{\text{SI}} = \langle E_k \rangle_{\text{SI}}/c$ , see Table 1.

		SI Z=2		SI		SI Z=2	
		$c_{1,2,3}=1$		$c_{1,2,3}=0$		$c_1=0, c_{2,3}=1$	
$I$ ( $\times 10^{15} \text{Wcm}^{-2}$ )	$\langle p_y \rangle$	$\langle E_k/c \rangle$	$\langle p_y \rangle$	$\langle E_k/c \rangle$	$\langle p_y \rangle$	$\langle E_k/c \rangle$	(†)
0.7	3.6	2.3	1.5	1.5	2.0	2.2	
He 1.3	6.1	4.4	3.4	3.4	3.3	4.4	
4.8	31	31	19	19	19	21	
0.05	3.2	1.6	1.3	1.3	1.8	1.6	
Xe 0.07	3.5	2.5	2.1	2.1	2.4	2.4	
0.22	11	12	9.9	9.9	9.1	11	

(†) Average momentum and kinetic energy given in  $\times 10^{-3}$  a.u.

**Table 1 | Single ionization results for Xe and He.**

Next,  $\langle p_y \rangle_{\text{SI}}$  and  $\langle E_k \rangle_{\text{SI}}$  are computed with the 3D-SMND model fully accounting for all Coulomb forces and the presence of the initially bound electron in driven He and Xe, i.e.  $c_1 = c_2 = c_3 = 1$  with  $Z = 2$ . The tunneling electron is the one that is mostly singly ionizing. In Fig. 2, we show that, for He,  $\langle p_y \rangle_{\text{SI}}$  varies from 0.0036 a.u. to 0.031 a.u. at intensities  $0.7\text{-}4.8 \times 10^{15}$   $\text{Wcm}^{-2}$ . For Xe,  $\langle p_y \rangle_{\text{SI}}$  varies from 0.0032 a.u. to 0.011 a.u. at intensities  $0.5\text{-}2.2 \times 10^{14}$   $\text{Wcm}^{-2}$ . In Table 1, it is shown that  $\langle p_y \rangle_{\text{SI}}$  and  $\langle E_k \rangle_{\text{SI}}/c$  when obtained with the full model do not differ by more than a factor of 3 from the values obtained

when all Coulomb forces are switched-off. Thus, the simple model yields the correct order of magnitude for  $\langle p_y \rangle_{\text{SI}}$ . It is also shown in Table 1, that with all Coulomb forces accounted for,  $\langle p_y \rangle_{\text{SI}}$  is no longer equal to  $\langle E_k \rangle_{\text{SI}}/c$  both for driven He and for driven Xe. For the full model,  $\langle E_k \rangle_{\text{SI}}$  is no longer just the drift kinetic energy, mainly due to the interaction of the tunneling electron with the nucleus. Indeed, using the 3D-SMND model with this interaction switched off, i.e.  $c_1 = 0$  and  $c_2 = c_3 = 1$ ,  $\langle p_y \rangle_{\text{SI}}$  is roughly equal to  $\langle E_k \rangle_{\text{SI}}/c$ , see Table 1.  $\langle p_y \rangle_{\text{SI}}$  is also shown in Table 1 to be more sensitive than  $\langle E_k \rangle_{\text{SI}}$  to the interaction of the tunneling electron with the nucleus. Summarizing the results for single ionization, propagating classical trajectories with initial times determined by the ADK rate and all Coulomb forces switched-off yields the correct order of magnitude for  $\langle p_y \rangle_{\text{SI}}$ .

### $\langle p_y^1 + p_y^2 \rangle$ for double ionization of He and Xe

For double ionization, the average of the sum of the electron momenta along the propagation direction of the laser field  $\langle p_y^1 + p_y^2 \rangle_{\text{DI}}$ , is computed for He driven by an 800 nm laser field and for Xe driven by a 3100 nm laser field. The parameters of the laser fields are the same as the ones employed in the single ionization section for He and Xe. The double ionization results obtained in this work were computed with at least  $2 \times 10^5$  events and therefore the statistical error introduced is very small. The results are plotted in Fig. 3a for He at intensities  $0.7\text{--}4.8 \times 10^{15} \text{ Wcm}^{-2}$  and in Fig. 3b for Xe at intensities  $0.5\text{--}2.2 \times 10^{14} \text{ Wcm}^{-2}$ . The values obtained for  $\langle p_y^1 + p_y^2 \rangle_{\text{DI}}$  are quite unexpected. Specifically,  $\langle p_y^1 + p_y^2 \rangle_{\text{DI}}$  is found to be roughly an order of magnitude larger than twice  $\langle p_y \rangle_{\text{SI}}$ , with  $\langle p_y \rangle_{\text{SI}}$  computed in the previous section. For comparison, both  $\langle p_y^1 + p_y^2 \rangle_{\text{DI}}$  and  $2\langle p_y \rangle_{\text{SI}}$  are displayed in Fig. 3. It is shown that  $\langle p_y^1 + p_y^2 \rangle_{\text{DI}} \approx 8 \times 2\langle p_y \rangle_{\text{SI}}$  for He at  $1.3 \times 10^{15} \text{ Wcm}^{-2}$ , while  $\langle p_y^1 + p_y^2 \rangle_{\text{DI}} \approx 13 \times 2\langle p_y \rangle_{\text{SI}}$  for Xe at  $7 \times 10^{13} \text{ Wcm}^{-2}$ . For  $1.3 \times 10^{15} \text{ Wcm}^{-2}$  and 800 nm  $\beta_0 = 0.18$  a.u., while for  $7 \times 10^{13} \text{ Wcm}^{-2}$  and 3100 nm  $\beta_0 = 0.58$  a.u.. Thus,  $\langle p_y^1 + p_y^2 \rangle_{\text{DI}}/2\langle p_y \rangle_{\text{SI}}$  is found to be maximum at intensities considerably smaller than the intensities corresponding to  $\beta_0 \approx 1$  a.u., i.e. the criterion for the onset of magnetic field effects [4, 5]. This is shown in Fig. 1. Moreover, unlike  $\langle p_y \rangle_{\text{SI}}$  which increases with increasing intensity as expected [10],  $\langle p_y^1 + p_y^2 \rangle_{\text{DI}}$  after reaching a maximum decreases with increasing intensity for the range of intensities currently considered (Fig. 3a,b). What is the mechanism responsible for this pattern? We answer this question in what follows.

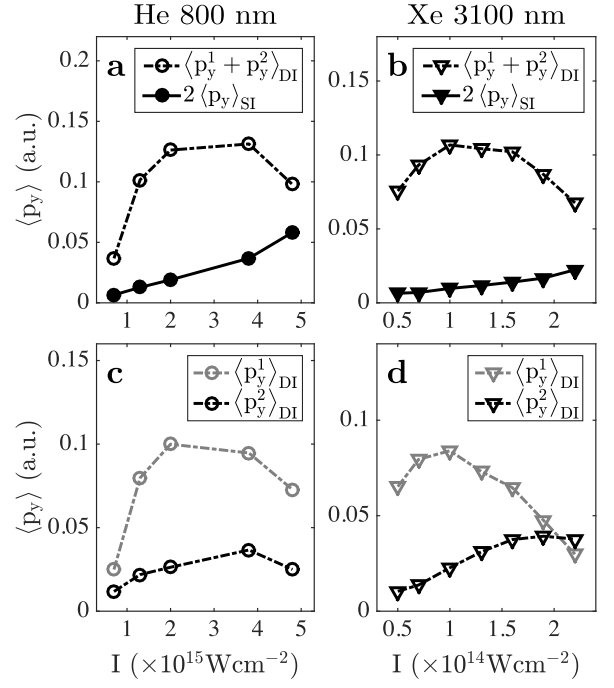


**Figure 3 | Double ionization of He and Xe.**  $\langle p_y^1 + p_y^2 \rangle_{\text{DI}}$  and  $2\langle p_y \rangle_{\text{SI}}$  are plotted as a function of intensity in (a) for He driven by an 800 nm laser field and in (b) for Xe driven by a 3100 nm laser field.  $\langle p_y^1 \rangle_{\text{DI}}$  and  $\langle p_y^2 \rangle_{\text{DI}}$  are plotted as a function of intensity in (c) for He driven by an 800 nm laser field and in (d) for Xe driven by a 3100 nm laser field.

### Recollision probing magnetic field effects

The average electron momentum along the propagation direction is non zero when the magnetic field component of the Lorentz force  $\mathbf{F}_B$  is accounted for. This force increases with increasing intensity—increasing strength of the magnetic field—and with increasing velocity along the direction of the electric field.  $\langle p_y^1 + p_y^2 \rangle_{\text{DI}}$  is found to be maximum at  $1.3 \times 10^{15} \text{ Wcm}^{-2}$  for 800 nm and at  $7 \times 10^{13} \text{ Wcm}^{-2}$  for 3100 nm, intensities where the strength of the magnetic field is not large. It then follows that it must be the velocities of the two escaping electrons that are significantly larger at these intensities than at the higher intensities considered in this work. Large electron velocities at intermediate intensities are a result of strong electron-electron correlation, i.e. of the rescattering mechanism [14]. In the rescattering scenario after electron 1 tunnels in the field-lowered Coulomb potential it accelerates in the strong laser field and can return to the core and undergo a collision with the remaining electron [14]. In what follows evidence is provided that the large values of  $\langle p_y^1 + p_y^2 \rangle_{\text{DI}}$  are due to recollisions. Specifically, it is shown that recollisions are strong resulting in overall large electron velocities roughly at the intensities where  $\langle p_y^1 + p_y^2 \rangle_{\text{DI}}$  is maximum. It is also shown that recollisions are soft resulting in overall smaller velocities



at higher intensities where  $\langle p_y^1 + p_y^2 \rangle_{DI}$  is found to be smaller.

This transition from strong to soft recollisions is demonstrated in the context of He driven by an 800 nm laser field at intensities  $0.7 \times 10^{15} \text{ Wcm}^{-2}$ ,  $2.0 \times 10^{15} \text{ Wcm}^{-2}$  and  $3.8 \times 10^{15} \text{ Wcm}^{-2}$ . To do so, an analysis of the doubly ionizing events is performed. In Fig. 4, the distribution of the tunneling and recollision times is plotted. As expected, for the smaller intensities (Fig. 4a1,b1), electron 1 tunnel-ionizes at times around the extrema of the laser field. For  $3.8 \times 10^{15} \text{ Wcm}^{-2}$  (Fig. 4c1) the electric field is sufficiently strong so that electron 1 can tunnel-ionize at times other than the extrema of the field. The distribution of the recollision times is also plotted. This time is identified for each double ionizing trajectory as the time that the electron-electron potential energy  $1/|\mathbf{r}_1 - \mathbf{r}_2|$  as a function of time is maximum. For the smaller intensities the recollision times are centered roughly around  $\pm 2nT/3$ , with  $n$  an integer and  $T$  the period of the laser field, as expected from the rescattering model [14] (Fig. 4a2,b2). At  $3.8 \times 10^{15} \text{ Wcm}^{-2}$  the recollision times shift and are centered around the extrema of the laser field (Fig. 4c2). This shift of the recollision times signals a transition from strong to soft recollisions [29]. This transition is further corroborated by the average kinetic energy of each electron,  $\langle E_k^{1,2} \rangle$ , plotted in Fig. 4 as a function of time; zero time is set equal to the recollision time of each double ionizing trajectory. For smaller intensities,  $\langle E_k^{1,2} \rangle$  changes sharply at the recollision time (Fig. 4a3,b3). The change in  $\langle E_k^{1,2} \rangle$  is much smaller at  $3.8 \times 10^{15} \text{ Wcm}^{-2}$  (Fig. 4c3). The above results show that for the smaller intensities electron 1 tunnel-ionizes around the extrema of the field. It then returns to the core, roughly when the electric field is small, with large velocity and undergoes a recollision with electron 2 transferring a large amount of energy (strong recollision). The velocities of both electrons along the direction of the elec-

tric field are determined mainly by the vector potential at the recollision time. Thus, both electrons escape mainly either parallel or antiparallel to the electric field. Indeed, this is the pattern seen in the plots of the correlated momenta along the direction of the electric field in Fig. 4a5,b5 where the highest density is in the first and third quadrants. The correlated momenta are plotted in units of  $\sqrt{2U_p}$ , with  $U_p$  the ponderomotive energy equal to  $E_0^2/(4\omega^2)$ . These patterns of the correlated momenta are consistent with direct double ionization, that is, with both electrons ionizing shortly after recollision takes place [30]. Indeed, analyzing the double ionizing events it is found that for He at  $0.7 \times 10^{15} \text{ Wcm}^{-2}$  direct double ionization contributes 80%. Delayed double ionization events contribute 20%. In delayed double ionization, also known as RESI [30, 31], one electron ionizes soon after recollision takes place, while the other electron ionizes with a delay [21]. In contrast, at the higher intensity of  $3.8 \times 10^{15} \text{ Wcm}^{-2}$ , electron 1 tunnel-ionizes after the extrema of the laser field. It then follows a short trajectory and returns to the core when the electric field is maximum with small velocity. Electron 1 transfers a small amount of energy to electron 2 (soft recollision). The velocities of electron 1 and 2 along the direction of the electric field are determined mostly by the values of the vector potential at the tunneling and recollision times, respectively. As a result, the two electrons can escape opposite to each other along the direction of the electric field. This pattern is indeed seen in the plots of the correlated momenta in Fig. 4c5 with high density in the second and fourth quadrants. This antiparallel pattern was predicted in the context of strongly-driven  $N_2$  with fixed nuclei [29]. It was also seen in the case of Ar driven by intense ultra-short laser fields [22] in agreement with experiment [23]. A similar analysis for Xe driven at 3100 nm is performed (not shown). Similar results are obtained. It is found that for driven Xe strong recollisions transition to soft ones roughly around  $22 \times 10^{13} \text{ Wcm}^{-2}$ .

$I (\times 10^{15} \text{ Wcm}^{-2})$	NSDI $c_{1,2,3}=1, Z=2$				NSDI $c_{1,2,3}=0$				
	$\langle p_y^2 \rangle$	$\langle E_k^2/c \rangle$	$\langle p_y^1 \rangle$	$\langle E_k^1/c \rangle$	$t_0 = t_{\text{rec}}, p_0^1 = p_{\text{rec}}^1, p_0^2 = p_{\text{rec}}^2$	$\langle p_y^2 \rangle$	$\langle E_k^2/c \rangle$	$\langle p_y^1 \rangle$	$\langle E_k^1/c \rangle$ (†)
He	0.7	12	14	25	16	13	15	25	16
	1.3	22	22	80	21	24	24	82	20
	4.8	25	32	73	47	33	37	74	43
Xe	0.05	10	11	65	9	11	11	67	8
	0.07	14	13	80	10	15	14	81	9
	0.22	38	27	30	17	45	34	30	16

(†) Average momentum and kinetic energy given in  $\times 10^{-3}$  a.u.

**Table 2 | Double ionization results for Xe and He.**

For single ionization of He and Xe, it was shown that

using the tunneling times as the starting point, the 3D-

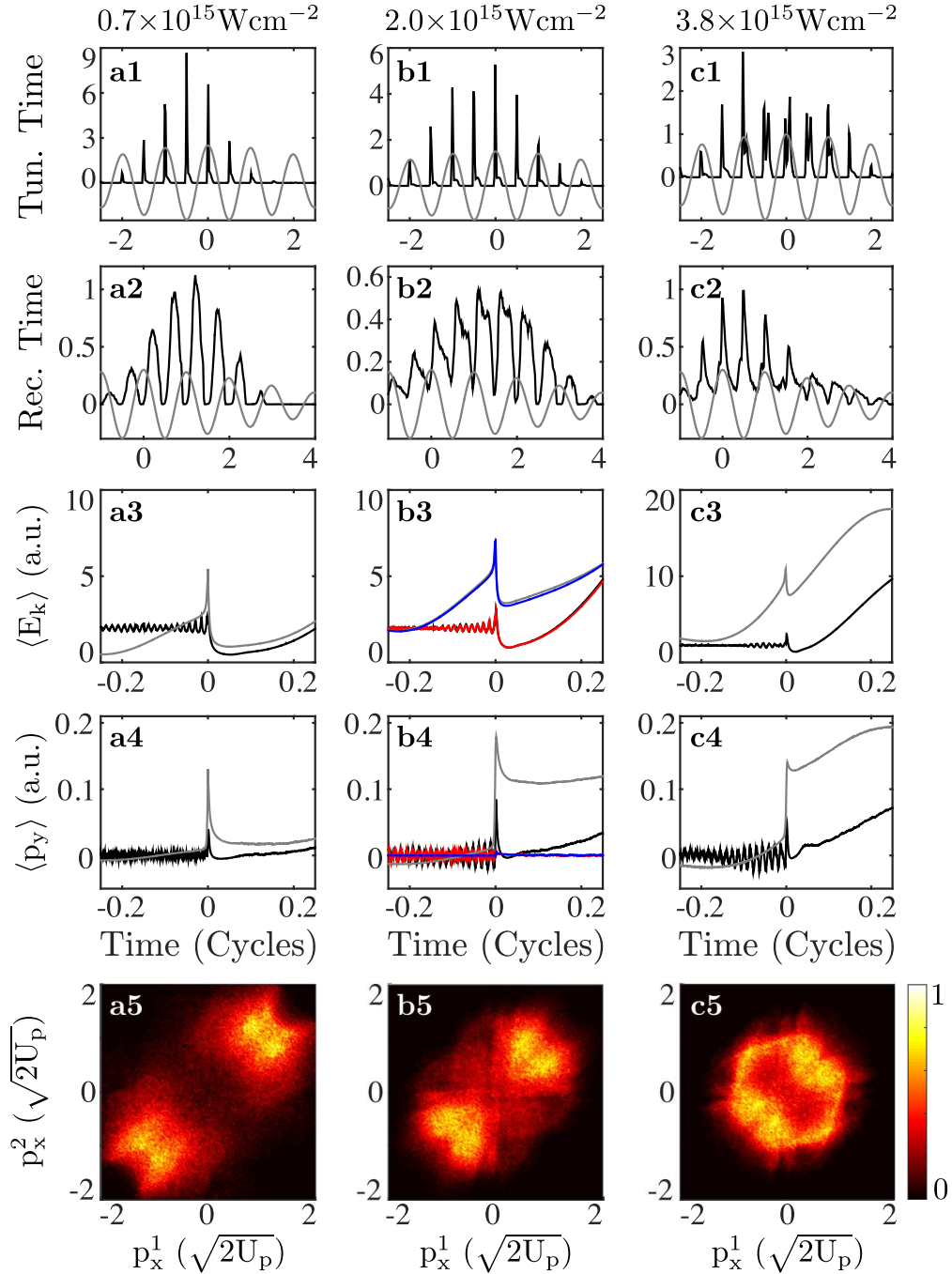


**Figure 4 | Recollision underlying double ionization of He driven at 800 nm.** The intensities considered are  $0.7 \times 10^{15} \text{ Wcm}^{-2}$ , denoted by (a),  $2.0 \times 10^{15} \text{ Wcm}^{-2}$ , denoted by (b), and  $3.8 \times 10^{15} \text{ Wcm}^{-2}$ , denoted by (c). The distribution of tunneling times (black line) is plotted in (a1), (b1) and (c1). The distribution of recollision times (black line) is plotted in (a2), (b2) and (c2). The electric field is denoted as a grey line in the plots of the tunneling and recollision times.  $\langle E_k \rangle$  (grey line) and  $\langle E_k^2 \rangle$  (black line) are plotted as a function of time in (a3), (b3) and (c3) with time zero set equal to the recollision time of each double ionizing event. For  $2.0 \times 10^{15} \text{ Wcm}^{-2}$ ,  $\langle E_k^1 \rangle$  (blue line) and  $\langle E_k^2 \rangle$  (red line) are also plotted in the absence of the magnetic field.  $\langle p_y^1 \rangle$  (grey line) and  $\langle p_y^2 \rangle$  (black line) are plotted as a function of time in (a4), (b4) and (c4) with time zero set equal to the recollision time of each double ionizing event. For  $2.0 \times 10^{15} \text{ Wcm}^{-2}$ ,  $\langle p_y^1 \rangle$  (blue line) and  $\langle p_y^2 \rangle$  (red line) are also plotted in the absence of the magnetic field. Correlated momenta along the direction of the electric field are plotted in (a5), (b5) and (c5).

SMND with all Coulomb forces switched-off yields the correct order of magnitude for  $\langle p_{y/SI}^1 \rangle$ . For double ionization of He and Xe, using the 3D-SMND model with all Coulomb forces switched-off and with initial conditions taken to be the recollision times and velocities,  $\langle p_{y/DI}^1 \rangle$  and  $\langle p_{y/DI}^2 \rangle$  are obtained and presented in Table 2. These values of  $\langle p_{y/DI}^1 \rangle$  and  $\langle p_{y/DI}^2 \rangle$  agree very well with the values obtained using the 3D-SMND model with all Coulomb forces accounted for, see Table 2. This agreement further supports that recollision is the main factor determining  $\langle p_y^1 + p_y^2 \rangle_{DI}$ .

Finally, in what follows, the electron that contributes the most to the maximum value of  $\langle p_y^1 + p_y^2 \rangle_{DI}$  is identified both for driven He and Xe.  $\langle p_{y/DI}^1 \rangle$  and  $\langle p_{y/DI}^2 \rangle$  are plotted as a function of time in Fig. 4, with time zero set equal to the recollision time of each double ionizing trajectory. It is shown in Fig. 4a4,b4,c4 that it is mainly  $\langle p_{y/DI}^1 \rangle$  that changes significantly at the recollision time. This change is more sharp for the smaller intensities (Fig. 4a4,b4). In Fig. 4b4, at intensity  $2.0 \times 10^{15}$  Wcm $^{-2}$ , it is also illustrated that in the absence of the magnetic field both  $\langle p_{y/DI}^1 \rangle$  and  $\langle p_{y/DI}^2 \rangle$  tend to zero with time, as expected. In addition, in Fig. 3c,d, for driven He and Xe, respectively,  $\langle p_{y/DI}^1 \rangle$  and  $\langle p_{y/DI}^2 \rangle$  are plotted as a function of intensity. It is seen that  $\langle p_{y/DI}^1 \rangle$  and  $\langle p_y^1 + p_y^2 \rangle_{DI}$  have maxima around the same intensities. At these intensities  $\langle p_{y/DI}^1 \rangle$  is significantly larger than  $\langle p_{y/DI}^2 \rangle$ . Thus,  $\langle p_{y/DI}^1 \rangle$ —the average momentum of the tunneling electron—is the one affected the most by strong recollisions.

## DISCUSSION

It was shown that the average sum of the electron momenta along the propagation direction of the laser field has large values at intensities where strong recollisions underlie double ionization. This is an unexpected result. For He driven by a near-infrared laser field and for Xe driven by a mid-infrared laser field, the intensities where the average sum of the electron momenta along the propagation direction of the laser field is maximum are smaller than the intensities where magnetic field effects are predicted to be large. Thus, recollision probes magnetic field effects at smaller intensities than expected. However, it can also be stated that a magnetic field probes strong recollisions through the measurement of the sum of the electron momenta along the propagation direction of the laser field. It is expected that the findings reported in this work will serve as a motivation for future studies. Such studies can identify, for instance, the effect the magnetic field has on the different mechanisms of non-sequential double ionization, i.e. on direct and delayed double ionization and the wavelengths where the magnetic field has the largest effect on recollisions.

## ACKNOWLEDGMENTS

A.E. is grateful for fruitful discussions with Paul Corkum. She also acknowledges the EPSRC grant no. J0171831 and the use of the computational resources of Legion at UCL.

## AUTHOR CONTRIBUTIONS

A.E. conceived the idea for the theoretical work, derived the theoretical framework and contributed many of the codes used for the computations. T. M. contributed some of the codes used for the computations, performed the computations and contributed to the analysis of the results.

- 
- [1] K. T. Taylor, J. S. Parker, D. Dundas and K. J. Meharg *J. Mod. Opt.* **54**, 1959 (2007).
  - [2] A. Becker, R. Dörner and R. Moshhammer *R. J. Phys. B* **38**, S753 (2006).
  - [3] D. B. Milošević, G. G. Paulus, D. Bauer, and W. Becker, *J. Phys. B* **39**, R203 (2006).
  - [4] H. R. Reiss, *Phys. Rev. Lett.* **101**, 043002 (2008).
  - [5] H. R. Reiss, *J. Phys. B.* **47**, 204006 (2014).
  - [6] S. Palaniyappan, A. DiChiara, E. Chowdhury, A. Falkowski, G. Ongadi, E. L. Huskins, and B. C. Walker, *Phys. Rev. Lett.* **94**, 243003 (2005).
  - [7] C. C. Chirilă, N. J. Kylstra, and R. M. Potvliege and C. J. Joachain, *Phys. Rev. A* **66**, 063411 (2002).
  - [8] M. W. Walser, C. H. Keitel, A. Scrinzi, and T. Brabec, *Phys. Rev. Lett.* **85**, 5082 (2000).
  - [9] S. Chelkowski, A. D. Bandrauk, and P. B. Corkum, *Phys. Rev. Lett.* **113**, 263005 (2014).
  - [10] S. Chelkowski, A. D. Bandrauk, and P. B. Corkum, *Phys. Rev. A* **92**, 051401 (R) (2015).
  - [11] A. S. Titi and G. W. F. Drake, *Phys. Rev. A* **85**, 041404(R) (2012).
  - [12] I. A. Ivanov, *Phys. Rev. A* **91** 043410 (2015).
  - [13] C. T. L. Smeenk, L. Arissian, B. Zhou, A. Mysyrowicz, D. M. Villeneuve, A. Staudte, and P. B. Corkum, *Phys. Rev. Lett.* **106**, 193002 (2011).
  - [14] P. B. Corkum, *Phys. Rev. Lett.* **71**, 1994 (1993).
  - [15] B. Wolter, M. G. Pullen, M. Baudisch, M. Sciafani, M. Hemmer, A. Senftleben, C. D. Schröter, J. Ullrich, R. Moshhammer, and J. Biegert, *Phys. Rev. X* **5**, 021034 (2015).
  - [16] A. Ludwig, J. Maurer, B. W. Mayer, C. R. Phillips, L. Gallmann, and U. Keller, *Phys. Rev. Lett.* **113**, 243001 (2014).
  - [17] A. Emmanouilidou, *Phys. Rev. A* **78**, 023411 (2008).
  - [18] J. S. Parker, B. J. S. Doherty, K. T. Taylor, K. D. Schultz, C. I. Bлага, and L. F. Di Mauro, *Phys. Rev. Lett.* **96**, 133001 (2006).
  - [19] A. Staudte, C. Ruiz, M. Scröffler, S. Scrössler, D. Zeidler, Th. Weber, M. Meckel, D. M. Villeneuve, P. B. Corkum, A. Becker, and R. Dörner, *Phys. Rev. Lett.* **99**, 263002 (2007).

- [20] A. Rudenko, V. L. B. de Jesus, Th. Ergler, K. Zrost, B. Feuerstein, C. D. Schroter, R. Moshhammer, and J. Ullrich, *Phys. Rev. Lett.* **99**, 263003 (2007).
- [21] A. Emmanouilidou, J. S. Parker, L. R. Moore, and K. Taylor, *New J. Phys.* **13**, 043001 (2011).
- [22] A. Chen, M. Kübel, B. Bergues, M. F. Kling and A. Emmanouilidou in preparation.
- [23] M. Kübel, C. Burger, N. G. Kling, T. Pischke, L. Beaufore, I. Ben-Itzhak, G. G. Paulus, J. Ullrich, T. Pfeifer, R. Moshhammer, M. F. Kling, and B. Bergues, *Phys. Rev. A* **93**, 053422 (2016).
- [24] P. Kustaanheimo and E. Stiefel, *J. Reine Angew. Math.* **218**, 204 (1965).
- [25] L. D. Landau and E. M. Lifshitz, *Quantum Mechanics* (Pergamon Press, New York, 1977).
- [26] N. B. Delone and V. P. Krainov, *J. Opt. Soc. Am. B* **8**, 1207 (1991).
- [27] E. Yakaboylu, M. Klaiber, H. Bauke, K. Z. Hatsagortsyan, and C. H. Keitel, *Phys. Rev. A* **88**, 063421 (2013).
- [28] R. Abrines and I. C. Percival, *Proc. Phys. Soc. London* **88**, 861 (1966).
- [29] A. Emmanouilidou and A. Staudte, *Phys. Rev. A* **80**, 053415 (2009).
- [30] B. Feuerstein, R. Moshhammer, D. Fischer, A. Dorn, C. D. Schröter, J. Deipenwisch, J. R. Crespo Lopez-Urrutia, C. Höhr, P. Neumayer, J. Ullrich, H. Rottke, C. Trump, M. Wittmann, G. Korn, and W. Sandner, *Phys. Rev. Lett.* **87**, 043003 (2001).
- [31] R. Kopold, W. Becker, H. Rottke and W. Sandner, *Phys. Rev. Lett.* **85**, 3781 (2000).